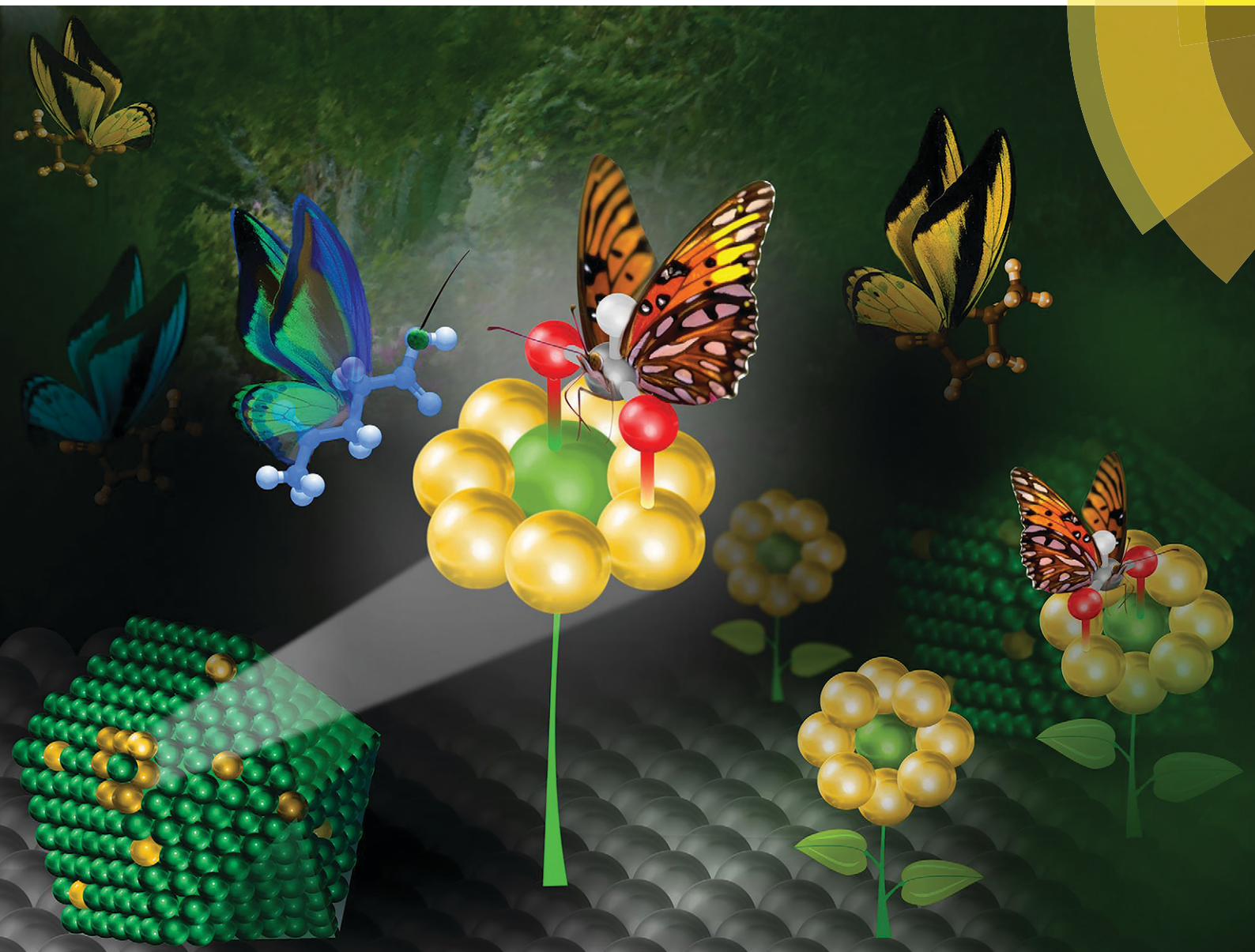# Catalysis Science & Technology

ROYAL SOCIETY
OF **CHEMISTRY**

PAPER
Agnieszka M. Ruppert, Carine Michel *et al.*
Supported gold–nickel nano-alloy as a highly efficient catalyst in levulinic
acid hydrogenation with formic acid as an internal hydrogen source

PAPER

Check for updates

Supported gold–nickel nano-alloy as a highly efficient catalyst in levulinic acid hydrogenation with formic acid as an internal hydrogen source†

Agnieszka M. Ruppert, [iD] *[a] Marcin Jędrzejczyk,[a] Natalia Potrzebowska,[a] Kamila Kaźmierczak,[a] Magdalena Brzezińska,[a] Olga Sneka-Płatek,[a] Philippe Sautet,[bde] Nicolas Keller,[c] Carine Michel [iD] *[b] and Jacek Grams[a]

Gamma-valerolactone (GVL) is one of the key products of future biorefineries. We show here for the first time the superior activity of Ni-based, Au doped catalysts in levulinic acid hydrogenation towards GVL using formic acid as a hydrogen source. Their performances are strongly influenced by the preparation method, and the highest GVL yield is achieved for bimetallic Au–Ni catalysts prepared *via* co-impregnation of both metallic salts with a reductive thermal treatment under hydrogen. The very high catalytic activity is explained by the use of DFT calculations and the extensive characterization of the catalyst surface and bulk properties. We highlight the pivotal role played by the incorporated isolated metallic Ni atoms within Au nanoparticles. The nano-alloy composition is determined. It allows establishment of a surface model of such an alloy, thanks to which the high activity can be explained by the presence of an optimum energetic span of FA adsorption. The existence of strong interaction between Au and Ni in a surface alloy, Au–Ni, favors selective and fast decomposition of formic acid into hydrogen that consequently facilitates strongly the combined hydrogenation process.

Introduction

In future biorefinery schemes, the crucial processes will be based on integrated biomass transformations towards high added value molecules with applications mainly for the trans-

[a] Institute of General and Ecological Chemistry, Faculty of Chemistry, Łódź University of Technology, ul. Żeromskiego 116, 90-924 Łódź, Poland. E-mail: agnieszka.ruppert@p.lodz.pl; Fax: +48426313128; Tel: +48426313106
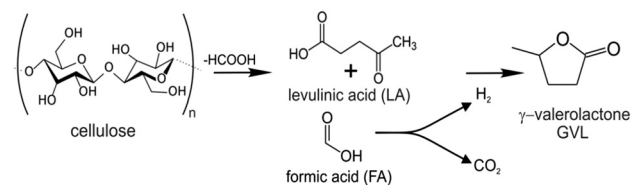
[b] Univ Lyon, Ens de Lyon, CNRS UMR 5182, Laboratoire de Chimie, Université Claude Bernard Lyon 1, F69342, Lyon, France. E-mail: carine.michel@ens-lyon.fr; Fax: +33472728080; Tel: +33472728847

[c] Institut de Chimie et Procédés pour l'Energie, l'Environnement et la Santé, ICPEES, CNRS, University of Strasbourg, 25 rue Becquerel, 67087, Strasbourg, France

[d] Department of Chemical and Biomolecular Engineering, University of California, Los Angeles (UCLA), Los Angeles, CA 90095, USA

[e] Department of Chemistry and Biochemistry, University of California, Los Angeles (UCLA), Los Angeles, CA 90095, USA

† Electronic supplementary information (ESI) available: Description of the preparation method of monometallic catalysts; details of characterization techniques; Fig. S1 shows the energy profiles for the formic acid decomposition through the carboxylate pathway on Au(111), Ni(111) and Au–Ni(111); Fig. S2 and S3 represent the computed structures of the intermediates and transition states on Au–Ni(111); Fig. S4 represents the computed Gibbs energy profiles for Au, Ni and Au–Ni surfaces with HCOOH dehydration *via* COOH; Fig. S5 shows the XPS spectra of the Au–Ni catalyst; Table S1 shows the activity of selected catalysts in FALA with gas phase selectivity; Table S2 shows the activity of the Au–Ni catalyst in re-use FALA tests; Table S3 shows ToF-SIMS analysis results of the catalyst surface. See DOI: 10.1039/c8cy00462e

portation sector. Gamma-valerolactone (GVL) and its downstream products such as 2-methyltetrahydrofuran (2-MTHF) or even valeric acid are typical examples of such high value molecules. GVL, besides being considered as a biofuel additive thanks to its low volatility, minimum toxicity and good stability,[1–3] has a lot of potential applications since it can be used as a solvent or for the synthesis of many molecules such as *e.g.* polymers with high thermal stability.[1,2]

GVL can be obtained through the catalytic hydrogenation of levulinic acid (LA). This reaction has been extensively studied with a focus on the catalyst used and on the hydrogenation conditions such as the reaction temperature, the solvent nature or the hydrogen pressure.[4–7] In most of those studies, an external source of hydrogen was used. A step forward in the integration of this transformation into a biorefinery involves the use of formic acid (FA) as an internal source of

Scheme 1 Hydrolytic hydrogenation of cellulose to γ-valerolactone with formic acid as an internal hydrogen source.

4318 | *Catal. Sci. Technol.*, 2018, **8**, 4318–4331

This journal is © The Royal Society of Chemistry 2018

hydrogen. Indeed, FA is formed in the hydrolysis of cellulose in an equimolar amount with LA, thus it is considered as a sustainable source of hydrogen (Scheme 1).[8]

The strategy of using an internal hydrogen from a reaction solvent or by-product (like formic acid) is very appealing but also challenging, since it requires efficient catalysis of both the dehydrogenation of FA and the hydrogenation of LA into GVL in one pot. This reaction is named hereafter the FALA reaction. It is well known that the conversion of LA into GVL under a pressure of external hydrogen can be catalyzed by supported Ru catalysts with high rates at temperatures lower than 100 °C.[9] However, these catalysts are not selective towards FA decomposition, so that they cannot be applied easily in the combined process.[10] Another difficulty is associated with the formation of side products, which potentially can block the other reactions. Typically, the FA decomposition may also yield CO through FA dehydration, which may strongly poison the catalyst.[11] Deng et al. showed that supported Ru catalysts get poisoned by formic acid or formate in a concentration higher than 10 mmol L^{-1}.[12]

Additionally, the use of non-noble metals as more stable and abundant catalysts appears to be an attractive sustainable solution. Yuan et al. proposed earth-abundant Cu-based catalysts able to efficiently convert an equimolar FA:LA aqueous mixture into GVL.[13] Based on the optimal conditions of the two separate reactions, they obtained a 100% selectivity to GVL at 180 °C but with a low LA conversion. Although this drawback was overcome by increasing the temperature to 200 °C, the catalytic hydrogenation of LA with FA as an internal hydrogen source remained however less efficient than that performed under external hydrogen pressure. In addition, a high loading of Cu (20 wt%) was required to reach this high activity. Also, Ni catalysts on various supports were tested in the FALA reaction in a continuous process at atmospheric pressure with increasing FA:LA ratio for improving the LA conversion.[14,15] However, those studies required, like the previous ones, the use of a high metal loading and an even higher reaction temperature (250 °C).

To further optimize the FALA reaction, the versatility of the supported bimetallic catalysts is a clear advantage as their properties could be tuned to a large extent. Both reactivity and adsorption properties of bimetallic particles are different than those of each metal considered separately.

As far as the use of bimetallic catalysts for the FALA reaction is concerned, except for the use of highly loaded Ni–Cu–SiO$_2$ nanocomposites in the vapor phase,[16] mainly bimetallic Ag–Ni catalysts were applied in the water phase.[17] Both high Ni loading (20%) and high reaction temperature (220 °C) were however required to obtain full LA conversion.

The desired catalyst should therefore possess the selective sites for converting FA to hydrogen and should be active for the subsequent hydrogenation process and at the same time resistant to impurities.

Here, we propose to apply Ni-based materials doped with a small amount of Au as highly efficient catalysts for the FALA reaction. It was reported that the activity of gold-based catalysts is strongly influenced by the preparation method. Indeed, on the one hand, the low activity of monometallic gold catalysts in levulinic acid hydrogenation with an external hydrogen source was reported,[18,19] while Luo et al. demonstrated that random nano-alloying of gold is a key approach for strongly improving its catalytic activity on a titania support compared to the monometallic counterparts.[18] On the other hand, Du et al. proposed a Au/ZrO$_2$ catalyst able to efficiently perform the FALA reaction at 180 °C, thanks to its ability to perform a fast and selective FA decomposition into CO$_2$ and H$_2$.[20]

Theoretical calculations for the hydrogenation of acetylene also confirmed that Au–Ni systems could be very active for hydrogenation reactions due to the reduction of the adsorption energy for acetylene.[21] The group of Norskov confirmed by theoretical investigations that these two metals are immiscible in the bulk but also showed that the formation of a 2D surface alloy was possible, in which gold is alloyed in the surface outermost layers of Ni(111). Au does not dissolve in the Ni bulk; therefore only a small amount of Au is necessary for Au–Ni formation.[22]

When it comes to formic acid decomposition so far there is also one proof of principle where the superior activity of Au–Ni was noted.[22] In this work, the efficiency of electrooxidation of formic acid was investigated on the Au–Ni alloy prepared by melting Au and Ni and was compared to pure gold. The high activity of this bimetallic system was attributed to Au–Ni alloy formation. This nice proof of principle stays however very far from our research where not only a different catalytic system is used (supported vs. bulk) but also another reaction (FALA vs. FA electrooxidation) with different reaction conditions is considered. The potential high activity of the Au–Ni alloy for FA decomposition is also predicted based on the volcano plot established by Yoo et al. using a combination of periodic density functional theory (DFT) calculation and microkinetics measurement.[23]

Here, we show for the first time the application of bimetallic Ni-based catalysts doped with a small amount of Au for the hydrogenation of LA with FA as an internal hydrogen source. We demonstrate the high activity of these catalysts in GVL production in comparison with some existing ones in the literature.[9,24–26] The influence of different synthesis approaches on the catalytic behavior of the bimetallic and monometallic systems in the FALA transfer hydrogenation and in the separate LA hydrogenation reaction has been explained by extensive characterization of the catalysts and DFT calculations applied to FA decomposition. They provided key insights into the high activity shown by the Au–Ni bimetallic systems in the FALA reaction compared to that of their mono-metallic counterparts, by highlighting the pivotal role played by isolated metallic Ni atoms within Au nanoparticles in feeding the LA hydrogenation catalysts with hydrogen. The use of the internal source of hydrogen is a more sustainable solution and therefore new stable catalysts are highly demanded. This work can shed the light on other hydrogenation reactions which use an external hydrogen source. The

This journal is © The Royal Society of Chemistry 2018

Catal. Sci. Technol., 2018, 8, 4318–4331 | 4319

findings could also broaden the possibility of applying the Au–Ni catalyst to other hydrogenation processes.

Experimental

γ-Al$_2$O$_3$ (Fluka, 136 m^2 g^{-1}) and TiO$_2$ (Aeroxide P25, 50 m^2 g^{-1}) were used as delivered.

Bimetallic catalyst synthesis

The Au–Ni bimetallic catalysts supported on γ-Al$_2$O$_3$ were prepared with a total metal content of 5 wt% and an Au : Ni wt ratio of 1 : 4, using aqueous solutions of Ni(NO$_3$)$_3$·6H$_2$O and HAuCl$_4$·4H$_2$O with a concentration of 8420 mg L^{-1} and 4599 mg L^{-1}, respectively.

The subsequent impregnation (SI) method. The γ-Al$_2$O$_3$ support was impregnated first with the aqueous nickel nitrate solution, and further dried at 120 °C for 2 h after complete evaporation of the solvent. The resulting powder was then calcined in air at 500 °C for 5 h (heating rate of 5 °C min^{-1}) and further impregnated with the chloroauric acid solution. After solvent evaporation, the sample was dried for 2 h at 120 °C and then calcined at 300 °C for 4 h in air flow (20 mL min^{-1}) with a heating rate of 10 °C min^{-1}, and further reduced in hydrogen flow (60 mL min^{-1}) at 300 °C for 1 h with a heating rate of 2 °C min^{-1}. This sample is labelled as Au–Ni$_{(SI)}$/γ-Al$_2$O$_{3(C)}$.

An analogous sample denoted as Au–Ni$_{(SI)}$/γ-Al$_2$O$_3$ was also prepared by direct reduction of the dried sample under hydrogen flow at 300 °C for 1 h with a heating rate of 2 °C min^{-1}, with no intermediate oxidation step.

The deposition–precipitation (DP) method. The γ-Al$_2$O$_3$ support was impregnated under reflux at 80 °C with a mixture of both metal precursor solutions supplemented with dropwise addition of urea as a precipitating agent to achieve a urea concentration of 0.42 mol L^{-1}. Afterwards the suspension was cooled down to room temperature and vacuum filtered, and the catalyst powder was dried at 120 °C for 2 h. The catalyst was then calcined at 300 °C for 4 h in air flow (20 mL min^{-1}) with a heating rate of 10 °C min^{-1}, and further reduced in hydrogen flow (60 mL min^{-1}) at 300 °C for 1 h with a heating rate of 2 °C min^{-1}. This sample is labeled as Au–Ni$_{(DP)}$/γ-Al$_2$O$_{3(C)}$.

An analogous sample denoted as Au–Ni$_{(DP)}$/γ-Al$_2$O$_3$ was also prepared by direct reduction of the dried sample under hydrogen flow at 300 °C, with no intermediate oxidation step.

The co-impregnation (CI) method. After addition of γ-Al$_2$O$_3$ to 250 mL of aqueous solution of the metal precursors, the resulting suspension was sonicated first for 3 h at room temperature (at 35 kHz, 320 W) and further at 80 °C for 7 h till complete evaporation of the solvent, before the obtained powder was dried at 120 °C for 2 h. The catalyst was then calcined at 300 °C for 4 h in air flow (20 mL min^{-1}) with a heating rate of 10 °C min^{-1}, and further reduced in hydrogen flow (60 mL min^{-1}) at 300 °C for 1 h with a heating rate of 2 °C min^{-1}. This sample is labeled as Au–Ni$_{(CI)}$/γ-Al$_2$O$_{3(C)}$.

An analogous sample denoted as Au–Ni$_{(CI)}$/γ-Al$_2$O$_3$ was also prepared by direct reduction of the dried sample under hydrogen at 300 °C, with no intermediate oxidation step.

The chemical reduction (CR) method. After addition of γ-Al$_2$O$_3$ to 250 mL of aqueous solution of the metal precursors, the resulting suspension was first sonicated for 1 h at room temperature (at 35 kHz, 320 W) before chemical reduction of the salt which was achieved *via* the addition of a 5-fold excess of NaBH$_4$ for 15 min. Then the suspension was vacuum filtered, washed with distilled water (500 mL) and finally dried at 80 °C for 12 h. This sample is labelled as Au–Ni$_{(CR)}$/γ-Al$_2$O$_3$.

The core–shell structure preparation method by consecutive chemical reduction. First, a nickel nitrate aqueous solution was mixed with a 10 wt% aqueous solution of polyvinyl alcohol (PVA, M_w 9.000–10.000, Sigma Aldrich, 80% hydrolyzed) with a PVA/Ni molar ratio of 5. The solution was adjusted to pH = 1 *via* the addition of concentrated nitric acid. The γ-Al$_2$O$_3$ support was further added to the solution, and the obtained mixture was stirred (1000 rpm) for 1 h at room temperature, before chemical reduction of the Ni salt occurred *via* addition of a 5-fold excess of NaBH$_4$ for 15 min.

Further, a similar HAuCl$_4$–PVA aqueous solution was prepared in 50 mL of distilled water by mixing HAuCl$_4$·4H$_2$O and a 10% aqueous solution of PVA to get a PVA/Au molar ratio of 5. It was maintained under stirring (1000 rpm) for 10 min at room temperature, before being added to the reduced Ni/γ-Al$_2$O$_3$ aqueous suspension and mixed for 1 h (1000 rpm). A second chemical reduction step occurred *via* further addition of a 5-fold excess of NaBH$_4$; the resulting suspension was maintained under vigorous stirring (1000 rpm) for 24 h. Then the powder was separated from the solution by vacuum distillation and washed with distilled water before it was finally dried overnight at 80 °C. This sample is labelled as Ni@Au.

The detailed preparation of the Au/γ-Al$_2$O$_3$, Ni/γ-Al$_2$O$_3$, Ru/TiO$_2$ and Ru/ZrO$_2$ monometallic counterparts used as reference catalysts is described in the ESI.†

Catalytic tests

Levulinic acid hydrogenation. In a typical levulinic acid (LA) hydrogenation experiment, 1 g of LA, 0.3 g of catalyst and 30 mL of water were combined in a stainless steel autoclave (Berghof, Germany), equipped with a Teflon insert allowing a reaction volume of 45 mL. The reactor was pressurized with H$_2$ to 10 bar and the temperature was maintained at 190 °C for 2 h. At the end of the reaction, the reactor was cooled down, the remaining pressure was released and the reaction mixture was centrifuged to separate the solid catalyst and the product solution.

LA hydrogenation with formic acid as a hydrogen source (FALA). In a typical LA hydrogenation experiment, 1 g of LA, 0.4 mL of FA, 0.6 g of catalyst and 30 mL of water were combined in a stainless steel autoclave (Berghof, Germany), equipped with a Teflon insert allowing a reaction volume of 45 mL. The temperature was maintained at 190 °C for 2 h. At

the end of the reaction, the reactor was cooled down, the remaining pressure was released and the reaction mixture was centrifuged to separate the catalyst and the product solution.

Reaction product analysis. Gaseous products were analyzed using a gas chromatograph (VEB Chromatrom, Berlin) equipped with a TCD detector. Argon was used as the carrier gas with a flow rate of 15 mL min^{-1} and the injections were performed with a volume of 2 mL. Liquid products were analyzed using a high-performance liquid chromatograph (Agilent Technologies 1260 Infinity, Perlan Technologies) equipped with a refractive index detector and a Rezex ROA column; 0.0025 mol L^{-1} H$_2$SO$_4$ was used as an eluent.

Computational details

Spin polarized periodic density functional theory (DFT) calculations were carried out with the Vienna *ab initio* simulation package (VASP).[27] The exchange–correlation energy and potential were calculated with the generalized gradient approximation (GGA) using the PBE functional[28] and including the dDsC dispersion correction,[29,30] a combination recently benchmarked against experimental adsorption energies.[31] A tight convergence of the plane-wave expansion was obtained with a cut-off of 400 eV. The electron–ion interactions were described by the projector augmented wave method (PAW).[32,33]

Close-packed (111) monometallic (Au and Ni) and bimetallic surfaces were modelled by a four-layer slab, separated by at least 10 Å of vacuum and using a $p(3 \times 3)$ supercell. In agreement with the characterization reported below (see TEM), the Au–Ni surface is modelled by a single atom alloy where one atom of the topmost layer of Au(111) is replaced by a Ni atom. A Monkhorst–Pack mesh of $3 \times 3 \times 1$ K-points for monometallic Au and bimetallic Au–Ni surfaces and $5 \times 5 \times 1$ K-points for the monometallic Ni surface were used for the 2D Brillouin zone integration to achieve a convergence in energy lower than 0.01 eV per atom.[34] Adsorption and reaction processes were realized on the upper surface of the slab. The two bottom layers were kept fixed at the bulk-truncated positions. The interatomic metal–metal distances are equal to 4.16 Å and 3.51 Å for Au and Ni, respectively (experimentally: 4.08 Å for Au and 3.52 Å for Ni). The coordinates of two uppermost layers and of the adsorbates were relaxed until forces were less than 0.015 eV Å^{-1}. The initially used magnetic moment value for Ni is equal to 0.61 μ_B per atom and it changed slightly to 0.66 μ_B.

The energies of pure slabs (G_{slab}), slabs with adsorbed species ($G_{ads/slab}$) and molecules in the gas phase (G_{gas}) are considered as Gibbs energies. We neglect the vibrational contribution to the Gibbs energy, thus G_{slab} and $G_{ads/slab}$ are approximated by their electronic energies (E_{ele}). For G_{gas} it is necessary to take into account the corrections for temperature and entropy. As the temperature value, we take 190 °C, which is the one used in catalytic tests. The rotational entropy corrections are computed using the rigid rotator and

the perfect gas approximations, using the experimental inertia moments for appropriate molecules, taken from the NIST database.[35]

$$G_{gas} \approx E_{ele} + nk_B T - T \cdot (S_t + S_r)$$

(n = 4 for non-linear molecules and n = 3.5 for linear molecules, k_B – Boltzmann constant, T – temperature, S_t and S_r – translational and rotational entropies, respectively).

The adsorption Gibbs energy G_{ads} is calculated as the difference between the Gibbs energy of the molecule adsorbed on the surface and that of a bare surface and molecule in the gas phase. A negative energy means a stabilizing adsorption.

Reaction paths have been studied, combining nudged elastic band procedures (NEB),[36,37] together with our local reaction path generator, OpenPath.[38] Transition states have been optimized using the dimer method,[39] and confirmed by the presence of a single imaginary frequency along the reaction coordinate.

To consider the effective reaction energetic barrier, the energy span model implemented by Kozuch and Shaik is applied.[40,41] The energetic span is defined as the difference of Gibbs energies between the TOF-determining intermediate (TDI) and the TOF-determining transition state (TDTS):

$$\delta G_{span} = \begin{cases} G_{TDTS} - G_{TDI} & \text{when TDTS appears after TDI} \\ G_{TDTS} - G_{TDI} + \Delta G_r & \text{when TDTS appears before TDI} \end{cases}$$

TDTS and TDI are the transition state and the intermediate of the catalytic cycle that maximize this Gibbs energy span.

Catalytic activity

The outstanding performance of bimetallic Au–Ni catalysts in the one-pot reaction

Table 1 shows the performances of selected catalysts in LA hydrogenation to GVL with FA as an internal hydrogen source. Various preparation methods were used and the supported Au–Ni bimetallic catalysts are compared with their monometallic counterparts.

The chemically reduced (CR) catalysts displayed activity only in the FA decomposition, and neither LA conversion nor GVL yield was obtained. While the chemically reduced monometallic gold showed only negligible activity in FA decomposition (25% in comparison with the 19% conversion obtained with the alumina support in a blank experiment), Ni$_{(CR)}$/γ-Al$_2$O$_3$ was much more active giving 52% FA conversion. The bimetallic Au–Ni$_{(CR)}$/γ-Al$_2$O$_3$ catalyst outperformed the monometallic ones, being the most active among the catalysts prepared by chemical reduction with an almost full conversion of FA (91%) and traces of LA conversion. A lower activity was achieved on the Ni@Au catalyst with a core shell structure obtained through successive chemical reductions, with a FA conversion of 59% and no LA conversion.

This journal is © The Royal Society of Chemistry 2018

Catal. Sci. Technol., 2018, **8**, 4318–4331 | **4321**

Table 1 Activity of mono- and bi-metallic supported catalysts in LA hydrogenation with FA as an internal hydrogen source (FALA)

Catalyst	FA conversion [%]	LA conversion [%]	GVL yield [%]
1% $Au_{(CR)}/\gamma$-Al_2O_3	25	0	0
4% $Ni_{(CR)}//\gamma$-Al_2O_3	52	0	0
Au–$Ni_{(CR)}/\gamma$-Al_2O_3	91	0	0
$Ni@Au$	59	0	0
Au–$Ni_{(CI)}/\gamma$-Al_2O_3	100	78	74
Au–$Ni_{(CI)}/\gamma$-$Al_2O_{3(C)}$	100	89	86
Au–$Ni_{(DP)}/\gamma$-Al_2O_3	100	47	43
Au–$Ni_{(DP)}/\gamma$-$Al_2O_{3(C)}$	100	76	72
Au–$Ni_{(SI)}/\gamma$-Al_2O_3	100	33	31
Au–$Ni_{(SI)}/\gamma$-$Al_2O_{3(C)}$	100	66	62
1% Au/γ-Al_2O_3	100	0	0
4% Ni/γ-$Al_2O_{3(C)}$	53	0	0
5% Ru/ZrO_2	79	0	0
5% Ru/TiO_2	100	8	4
γ-Al_2O_3	19	0	0

Reaction conditions: 190 °C; 2 h; 0.6 g of catalyst; 1 g of LA; 0.4 mL of FA and autogenic pressure.

The catalysts reduced by a high temperature reductive treatment showed a similar trend: all bimetallic catalysts are more active than the monometallic ones. But, in contrast to the chemically reduced ones, the bimetallic catalysts allow complete FA decomposition and even facilitate the subsequent LA hydrogenation.

The calcination played a pivotal role in the activity of the material, regardless of the initial step of preparation. Indeed, in the case of the catalysts prepared *via* the co-impregnation (Au–$Ni_{(CI)}/\gamma$-Al_2O_3), deposition–precipitation (Au–$Ni_{(DP)}/\gamma$-Al_2O_3) and subsequent impregnation (Au–$Ni_{(SI)}/\gamma$-Al_2O_3) methods, performing a calcination step before the final reduction at 300 °C enhanced both the LA conversion and the GVL yield. Among the three preparations, the subsequent impregnation yielded the lowest catalytic activity and the co-impregnation the highest one.

The most efficient catalyst is Au–$Ni_{(CI)}/\gamma$-$Al_2O_{3(C)}$ catalyst, with a LA conversion and a GVL yield of 89% and 86%, respectively, at full formic acid conversion. It achieves a significantly higher LA conversion and GVL yield than the reference catalysts, which are widely considered in the literature as the most active ones for LA hydrogenation using an external hydrogen source.[9,25,27] Ru/ZrO_2 cannot fully decompose FA in 2 h, and there is no LA conversion. On the Ru/TiO_2 catalyst, despite a full conversion of FA, almost no GVL was obtained.

Performances in LA hydrogenation

To rationalize the impact of the preparation method on the catalytic activity in the FALA reaction, assessing the activity towards the separate reactions is key. The FALA reaction was shown to follow a sequential mechanism: the LA hydrogenation can take place once the FA decomposition is complete.[10] That is why the activity performance in FA decomposition

can be estimated from the combined reaction (Table 1): the bimetallic catalysts outperform their monometallic counterparts, with Au being particularly poor at converting FA. On the other hand, to understand the activity in LA hydrogenation only, LA hydrogenation was conducted separately under external hydrogen pressure (Table 2). The catalyst series prepared *via* the co-impregnation and deposition–precipitation methods were selected for comparison tests with the monometallic counterparts, because they showed the highest activity among the bimetallic catalysts in the FALA reaction (with GVL yields of 89% and 76%, respectively, for samples calcined prior to reduction).

The difference between mono- and bimetallic catalysts at converting LA into GVL was even more clearly evidenced using external hydrogen: the bimetallic catalysts displayed much higher conversions. On the other hand, the modification of the synthesis did not influence significantly the LA conversion as well as the GVL yield. Indeed, the bimetallic catalysts prepared by various methods showed surprisingly similar performances, with a LA conversion and a GVL yield of 58–65% and 55–60%, respectively, while significant differences in GVL yield were clearly visible in the FALA reaction (Table 1). In addition, the ranking of the catalysts differs from the one obtained for the FALA reaction.

Characterization

X-ray diffraction (XRD) analysis

The diffraction patterns of the γ-Al_2O_3 support as well as of the reduced monometallic and bimetallic Au–Ni/Al_2O_3 catalysts are shown in Fig. 1. The XRD pattern of the bare support exhibits broad and weakly resolved diffraction peaks corresponding to cubic lattice γ-Al_2O_3 and attributed to the diffraction of the (111), (220), (311), (222), (400), (511), (440) and (444) planes at 2θ = 32.0°, 37.7°, 39.5°, 45.9°, 60.8°, 66.9° and 85.0°, respectively.[42,43]

For the Au/γ-$Al_2O_{3(C)}$ monometallic catalyst, additional peaks have been observed at 2θ = 38.3°, 44.4°, 64.6° and 77.6°, which are assigned to the diffraction of the (111), (200), (220) and (311) planes of metallic face-centered cubic Au particles, respectively.[44]

In the case of the Ni/γ-Al_2O_3 catalyst, no additional diffraction peaks were observed. The overlapping of the broad peak assigned to the (400) plane of γ-Al_2O_3 at 2θ = 45.9° with the

Table 2 Activity of mono- and bi-metallic supported catalysts in LA hydrogenation with an external hydrogen source

Catalyst	LA conversion [%]	GVL yield [%]
4% Ni/γ-$Al_2O_{3(c)}$	0	0
1% Au/γ-$Al_2O_{3(c)}$	5	5
Au–$Ni_{(CI)}/\gamma$-Al_2O_3	65	59
Au–$Ni_{(CI)}/\gamma$-$Al_2O_{3(c)}$	60	54
Au–$Ni_{(DP)}/\gamma$-Al_2O_3	62	60
Au–$Ni_{(DP)}/\gamma$-$Al_2O_{3(c)}$	58	55

Reaction conditions: 190 °C; p_0 H_2 = 10 bar; 2 h; 1 g of LA; 0.3 g of catalyst.
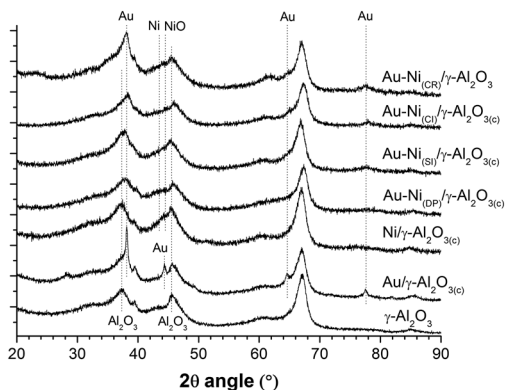
Fig. 1 Powder XRD pattern of the γ-Al$_2$O$_3$ support, the Ni/γ-Al$_2$O$_{3(C)}$ and Au/γ-Al$_2$O$_{3(C)}$ monometallic catalysts, and the bimetallic catalysts. JCPDS cards: γ-Al$_2$O$_3$ (04-0784), Au (65-2870), Ni (04-0850), and NiO (47-1049).

most intense peak of both Ni and NiO phases, *i.e.* at $2\theta = 44.5°$ and $2\theta = 43.3°$ for the (111) and (200) planes, respectively, led to a visible shoulder, as a fingerprint of the presence of supported Ni, although it was not possible to discriminate between its metallic or oxide nature.[45,46]

By contrast, the patterns recorded on bimetallic catalysts did not exhibit any clear shoulder in the Al$_2$O$_3$ diffraction peak at $2\theta = 45.9°$, probably due to a smaller crystallite size of the Ni-based phase, resulting from the preparation methods. No clear peak assigned to the metallic Au plane could be observed, due to the overlapping of its most intense peak, *i.e.* that of the (111) plane at $2\theta = 38.3°$, with that of the (311) plane of γ-Al$_2$O$_3$ at $2\theta = 37.7°$, as well as to the low intensity of the Au diffraction signals compared to the Au/γ-Al$_2$O$_3$ counterpart. However, the presence of metallic Au was revealed by the slight shift towards higher angles observed at $2\theta = 38.3°$, resulting from the peak overlap. This was confirmed by the appearance of the broad low intensity peak assigned to the diffraction of the (311) planes of metallic Au at $2\theta = 77.6°$. It could be noticed that the presence of metallic Au was less visible on the Au–Ni$_{(DP)}$/γ-Al$_2$O$_{3(C)}$ catalyst, and more visible on the Au–Ni$_{(CR)}$/γ-Al$_2$O$_3$ catalyst compared to the other bimetallic catalysts. Also, compared to the Au/γ-Al$_2$O$_3$ monometallic counterpart, the lower intensity of the diffraction signals could result probably from a smaller metallic Au particle size, or from a shorter coherent diffraction length.

ToF-SIMS analysis of the catalyst surface

In order to characterize the changes occurring on the surface of the catalysts after various preparation methods, ToF-SIMS measurements were performed (Table 3). The corresponding intensity ratios were calculated for chosen ions identified in the mass spectra collected from the catalyst surface.

The Ni : Au surface ratio depends strongly on the preparation method. Obviously its lowest value was identified for the core–shell catalyst, which proves that in that case gold is mainly present on the surface (Table 3, entry 9). Both the

co-impregnation and subsequent impregnation methods led to obtaining a similar Ni$^-$/Au$^-$ ratio in the range of 0.21–0.29 (Table 3, entries 2–3 and 6–7) whereas the chemical reduction method (that does not involve any thermal treatment) and the deposition–precipitation method led to a higher Ni$^-$/Au$^-$ ratio in the range of 0.40–0.51 (Table 3, entries 4–5 and 8).

During ToF-SIMS measurements, we observed as well the formation of Ni$_2$Au$^-$ ions. The formation of these Au–Ni species was however not noticed in the case of the mechanical mixture (entry 10). This suggests the presence of a surface alloy. Although in the case of Au–Ni metals the miscibility gap is too large that the formation of the alloy is only possible at very high temperatures like 810 °C,[47] a limited amount of Ni can 'dissolve' in Au or *vice versa* at much lower temperatures.[48] This means that for instance, Ni atoms may substitute Au atoms in the outermost atomic layers to form a so-called 'surface alloy'. The intensity of this Ni$_2$Au$^-$ ion that can be directly related to the formation of the surface alloy depends on the preparation method: the relative intensity of this ion to the total ions remains mostly in the range of 0.3–0.4×10^{-3} but a higher intensity was identified for catalysts prepared by impregnation (0.49×10^{-3}) and core shell (0.65×10^{-3}) methods (Table 3, entries 6 and 9). This stronger intensity of the Ni$_2$Au$^-$ ion is associated with a high intensity of the AuCl$_2^-$ ions. The association of gold atoms with chlorine probably facilitated the formation of the alloy by the modification of the electronic structure of gold.

When it comes to the changes of the Cl$^-$ ion intensity reported in Table 3 as the ratio of Cl$^-$/total ions, the highest concentration of residual Cl$^-$ ions is observed on the surface of the samples subjected to co-impregnation and subsequent impregnation (Table 3, entries 2–3 and 6–7). However only in the case of Au–Ni$_{(SI)}$/γ-Al$_2$O$_3$ catalysts was most of the chlorine associated with Au.

On the surface of the investigated catalysts, Au$_2^-$ ions were also identified, and in general the higher the intensity of such multiple ions, the larger the crystallites on average.[49] The Au$_2^-$/Au$^-$ ratio was the highest for the monometallic samples and the Ni@Au core–shell that should expose mainly Au at the surface. This is in agreement with the literature which suggests that the dispersion is higher in the case of bimetallic nanoparticles with respect to their monometallic counterparts.[43]

Temperature programmed reduction (TPR) analysis

The TPR profiles of the mono- and bimetallic catalysts before the final reductive step are presented in Fig. 2. As the highest temperature used for the catalyst preparation never exceeded 600 °C, the TPR profiles were recorded to that temperature. For the monometallic Au/Al$_2$O$_3$ catalyst calcined at 500 °C, almost no hydrogen uptake was observed. This can be related to the high calcination temperature that allows the complete decomposition of the Au precursor directly into metallic Au. In addition, Au$_2$O$_3$ is not stable[50] and residual surface

This journal is © The Royal Society of Chemistry 2018

Catal. Sci. Technol., 2018, **8**, 4318–4331 | **4323**

Table 3 Normalized intensity of selected ions calculated on the basis of the mass spectra collected from the surface of catalysts obtained by different preparation methods

Entry	Catalyst	Ni^-/Au^-	$AuCl_2^-/Au^-$	$Cl^-/total^-$	$Ni_2Au^-/total^-$ ($\times10^{-3}$)	Au_2^-/Au^- ($\times10^{-2}$)
1	1% Au/γ-Al$_2$O$_{3(c)}$	—	0.077	0.028	—	5.89
2	Au–Ni$_{(CI)}$/γ-Al$_2$O$_3$	0.21	0.050	0.113	0.29	2.86
3	Au–Ni$_{(CI)}$/γ-Al$_2$O$_{3(C)}$	0.24	0.034	0.076	0.32	2.99
4	Au–Ni$_{(DP)}$/γ-Al$_2$O$_3$	0.49	0.053	0.071	0.32	1.31
5	Au–Ni$_{(DP)}$/γ-Al$_2$O$_{3(C)}$	0.40	0.044	0.064	0.40	1.50
6	Au–Ni$_{(SI)}$/γ-Al$_2$O$_3$	0.22	1.348	0.132	0.49	2.76
7	Au–Ni$_{(SI)}$/γ-Al$_2$O$_{3(C)}$	0.29	0.241	0.133	0.30	2.72
8	Au–Ni$_{(CR)}$/γ-Al$_2$O$_3$	0.51	0.117	0.072	0.27	2.65
9	Ni@Au	0.02	0.632	0.060	0.65	6.52
10	1% Au/γ-Al$_2$O$_3$ + 4% Ni/γ-Al$_2$O$_3$	0.12	0.246	0.44	—	4.00

chlorine with a low reduction potential (−1.36 V) can help in reducing gold to its metallic state.[51] Further, no low temperature (<30 °C) hydrogen uptake was observed, which was already associated with the removal of oxygen atoms or of residual chlorine weakly adsorbed on the gold surface.[52] The formation of metallic gold under our conditions was also confirmed by XRD results.
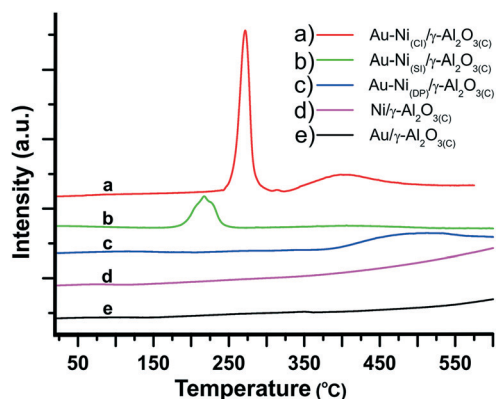
When it comes to monometallic Ni/Al$_2$O$_3$, the TPR baseline slightly rises with increasing temperature, which suggests that there is a small hydrogen uptake. It could come from the partially reduced NiO phase, due to the strong interaction with the alumina support and to the small size of particles (see XRD results). Indeed, for high Ni loadings (~20–50%), hydrogen uptake is observed in the temperature range of 200–350 °C and attributed to the reduction of the NiO bulk.[53] However, when deposited on a support, the reduction temperature can be shifted up to 450–600 °C or even much higher due to the existence of a strong interaction with the support.[54] The slight hydrogen uptake observed for 4% Ni/Al$_2$O$_3$ here could also be related to the reduction of nickel atoms incorporated into the alumina structure. At high temperatures during the catalyst treatment, incorporation of Ni atoms into the subsurface of the alumina support can occur. Indeed, spinel-like species have been identified in several alumina-supported catalysts like Ni, Au, Pd, and Pt, and exhibited usually high reduction temperatures, much higher than their respective oxides.[53,55,56] That is why in our case, we have probably a mixture of NiO$_x$ and Ni phases on the investigated catalysts. In the case of the bimetallic catalysts, the reducibility depends to a great extent on the preparation method that was used. The profile of Au–Ni$_{(DP)}$/γ-Al$_2$O$_{3(C)}$ was similar to that of monometallic nickel showing only one broad peak above 400 °C. In this case, the hydrogen uptake started at a lower temperature than for the monometallic Ni catalyst, suggesting the interaction of Ni in a different way with Al$_2$O$_3$ or with different species like Au species. In the case of the Au–Ni$_{(DP)}$/γ-Al$_2$O$_{3(C)}$ catalyst, the reduction of various alumina hydroxide species is also reported[57] (e.g. Au(OH)$_3$, [AuCl(OH)$_3$]$^-$ or [AuCl$_2$(OH)$_2$]$^-$ which are formed during preparation). For Au–Ni$_{(SI)}$/γ-Al$_2$O$_{3(C)}$, the hydrogen uptake peak is rather sharp with the maximum located at 210 °C, but still with a low intensity. The highest hydrogen uptake was observed for the Au–Ni$_{(CI)}$/γ-Al$_2$O$_{3(C)}$ catalyst, which is also the most active catalyst. For this catalyst, the TRP profile also strongly differed with the existence of two temperature regions for the reduction. The maximum hydrogen uptake was noted in the low temperature region, with a first maximum at 260 °C and a second one at 410 °C. The highest reduction temperatures that were observed for the Au–Ni$_{(CI)}$/γ-Al$_2$O$_{3(C)}$ catalyst can be associated with the strong interaction of Au and Ni, and with the small particle size of both metals, as suggested in the literature.[58,59]

X-ray photoelectron spectroscopy (XPS) analysis

Surface characterization has been performed by XPS in order to understand the nature of the active sites responsible for the high activity of the Au–Ni$_{(CI)}$/γ-Al$_2$O$_{3(C)}$ catalyst in the FALA reaction and to probe possible surface metal interactions. Fig. 3 shows both Ni 2p$_{3/2}$ and Au 4f regions of the XPS spectra recorded after *in situ* reduction at 300 °C under hydrogen of the Au–Ni$_{(CI)}$/γ-Al$_2$O$_{3(C)}$ catalyst, to avoid any surface re-oxidation of reduced nickel when exposed to air. The Ni 2p$_{3/2}$ orbital spectrum of the dried sample is reported for comparison.

In general, the Ni 2p$_{3/2}$ orbital spectra show a complex feature with a broad multi-contribution envelope, composed of the core level peaks and of several shake-up satellite peaks attributed to a multi-electron excitation and characteristic of Ni species in oxidized states.[60–62] However, by contrast to the dried sample, it could be seen from the spectra recorded on
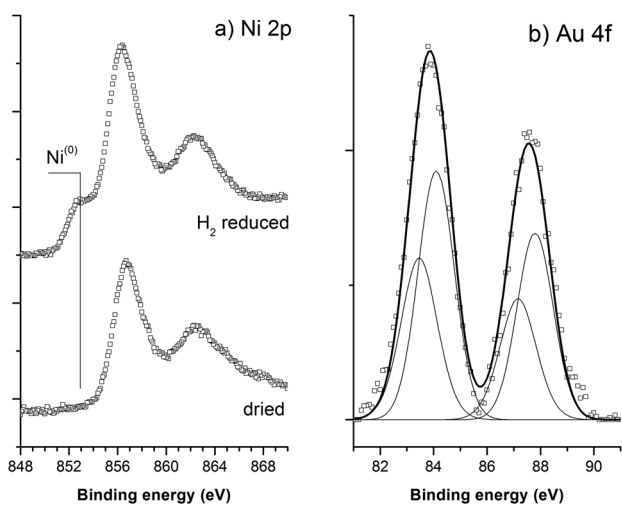

Fig. 2 TPR profile of the Au, Ni and Au–Ni catalysts.

4324 | *Catal. Sci. Technol.*, 2018, **8**, 4318–4331

This journal is © The Royal Society of Chemistry 2018

the catalyst after hydrogen treatment that both metallic and oxidized states of Ni co-exist within the supported nanoparticles. Indeed, the broad and complex envelop feature shown by both Ni $2p_{3/2}$ orbital spectra showed a contribution at 856.4 eV corresponding to Ni in oxidized states, while they differed with the appearance in the peak foot of a contribution at 852.9 eV assigned to metallic Ni.[16,63,64]

The Au 4f orbital XPS spectra of the Au–Ni$_{(CI)}$/γ-Al$_2$O$_{3(C)}$ catalyst exhibit two contributions, each of them as a doublet corresponding to Au $4f_{7/2}$–Au $4f_{5/2}$ spin–orbit components with a 3.7 eV spin orbit coupling constant. The low binding energy doublet at 83.5 eV and 87.2 eV was assigned to metallic gold, and a significant shift was observed towards lower binding energy with respect to the well-accepted value of 84.0 eV for bulk metallic gold.[16,65–68] We proposed that this resulted from the existence of metal–support interactions, which have been ascribed to a charge transfer in the substrate to nanometer-size metallic gold particles.[69–71] Indeed, it is well-known that the Au 4f electrons of surface gold atoms display a binding energy lower than that of bulk Au atoms. Rousset and co-workers have evidenced a 0.9 eV lower binding energy shift which was observed for 3 nm size Au particles on alumina.[69] They have reported that this energy shift strongly depended on the nature of the oxide support. Ealet and Gillet have correlated the charge transfer and the electronegativity of the supported metals.[72] The electronic interaction between the metal atoms and the surface cations can occur for metals such as gold with an electronegativity close to that of oxygen and higher than that of aluminium cations of the support. This results from the role of an electron acceptor played by gold – in competition with surface oxygen atoms – with respect to aluminium cations.

A higher binding energy contribution was observed at 84.1 eV and 87.8 eV, with a +0.6 eV shift when compared to the first metallic Au co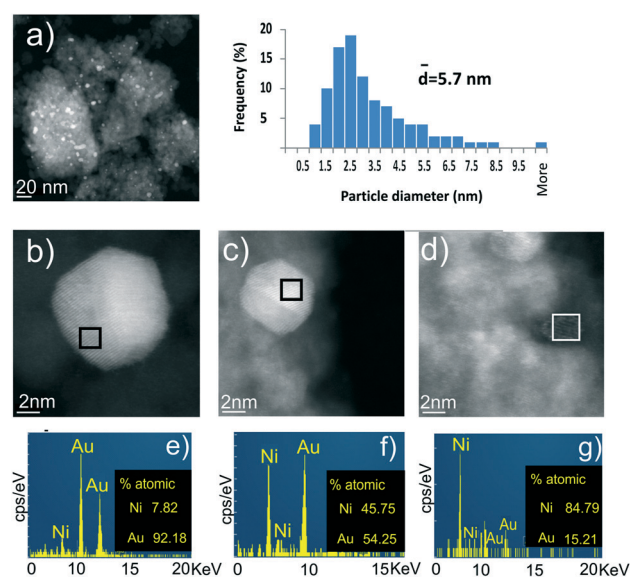ntribution. Such a high energy shift, strongly dependent on the support oxide nature, is usually assigned to Au$^{\delta+}$ species, and explained by a strong metal–oxide support interaction.[67] Considering that we proposed the existence of an electron transfer from the alumina support to supported Au, we hypothesized that this higher energy Au$^{\delta+}$ contribution came from metallic gold in direct interaction with metallic nickel within bimetallic Au–Ni particles,[73–75] as will be discussed later, with an electronic transfer from host metallic gold to guest nickel.

Transmission electron microscopy (TEM) images

In order to get deeper insight into the higher activity of the Au–Ni$_{(CI)}$/γ-Al$_2$O$_{3(C)}$ catalyst, STEM characterization was performed. Fig. 4 shows selected STEM images together with detailed EDX analyses and the derived nanoparticle size histogram. In the case of the Au–Ni$_{(CI)}$/γ-Al$_2$O$_{3(C)}$ catalyst, small particles were observed with a rather narrow distribution centered around an average particle size of 5.7 nm. The detailed EDX analysis of isolated single nanoparticles confirmed the bimetallic nature of the metal particles for this sample: Ni and Au stay in a very close contact with each other. A small contribution of Ni was in most of the cases observed within the well-defined Au metal particles, and estimated to be 10 atomic percent (Fig. 4). Besides this most frequent case, other nanoparticles with an equal contribution of both Ni and Au, or with a small content of Au vs. Ni, were also observed. Due to the usually amorphous nature of Ni nanoparticles, the latter case was the least frequently identified.

To check how the elements are distributed within the particle and to investigate if the observed bimetallic nature of

Fig. 3 (a) Ni $2p_{3/2}$ and (b) Au 4f regions of the XPS spectra recorded after *in situ* reduction under hydrogen of the Au–Ni$_{(CI)}$/γ-Al$_2$O$_{3(C)}$ catalyst. For comparison, the Ni $2p_{3/2}$ spectrum of the dried sample is reported.

Fig. 4 (a) STEM microscopy images recorded on the Au–Ni$_{(CI)}$/γ-Al$_2$O$_{3(c)}$ catalyst, with the derived nanoparticle size distribution histogram. STEM image with the corresponding EDX analysis, recorded on an isolated single nanoparticle with (b and e) a high Au/Ni atomic ratio, (c and f) a 50 : 50 Au/Ni atomic ratio and (d and g) a low Ni/Au atomic ratio reported.

This journal is © The Royal Society of Chemistry 2018

Catal. Sci. Technol., 2018, 8, 4318–4331 | 4325

the EDX spectra recorded with STEM analysis is due to the close presence of nanoparticles or to an intimate contact of Au and Ni within the particle, HRTEM images of a representative single nanoparticle were recorded (Fig. 5). The planes of the Au crystal were identified based on the analysis of respective reflexes (JCPDS No. 03-065-2870). The detailed EDX analysis taken on this nanoparticle evidenced the presence of both Au and Ni elements within isolated particles, with an 11:89 Ni:Au atomic contribution. This confirms the presence of the surface alloy, with Ni atoms 'dissolving' in the Au crystal. However, the opposite situation cannot be excluded.

Fig. 6 shows the STEM images of Au–Ni$_{(DP)}$/γ-Al$_2$O$_{3(C)}$ and Au–Ni$_{(DP)}$/γ-Al$_2$O$_3$ catalysts with the respective particle size histograms. Both catalysts showed smaller particle size of metals when compared to that of Au–Ni$_{(CI)}$/γ-Al$_2$O$_{3(C)}$, at 3.3 nm and 2.5 nm, respectively. However average nanoparticle sizes of 3–5 nm were reported[43,44,76] when a similar synthesis approach was applied. This observed dispersion remains in agreement with the literature that reported the strong dependence of the average particle on the preparation conditions and metal loading. Also, the size of Au–Ni can vary within a large range: very large nanoparticles (about 20 nm) can also be observed when the catalyst was subjected to a very long reductive treatment in hydrogen flow or when the catalyst was prepared *via* a subsequent impregnation procedure.[60]

The distribution of metal particles at the surface of the Au–Ni$_{(DP)}$/γ-Al$_2$O$_{3(C)}$ and Au–Ni$_{(DP)}$/γ-Al$_2$O$_3$ catalysts is homogeneous. However, contrary to what was observed for the Au–Ni$_{(CI)}$/γ-Al$_2$O$_3$ catalyst, large agglomerates of amorphous nickel were noted, particularly in the case of the Au-Ni$_{(DP)}$/γ-Al$_2$O$_3$ sample. Probably in this case, the crystallization process did not occur to a large extent, which is why a very small amount of crystalline nanoparticles (both Au and Ni) was identified in this sample. This is in agreement with XRD, for which Au crystallites are well visible in the Au–Ni$_{(CI)}$/γ-Al$_2$O$_{3(C)}$ spectra, by contrast to what was observed for the Au–Ni$_{(DP)}$/γ-Al$_2$O$_{3(C)}$ catalyst.

Theoretical study

According to our catalytic tests, the ability of the catalyst to rapidly perform formic acid decomposition seems to be decisive for the efficiency of the one-pot process. To better under-
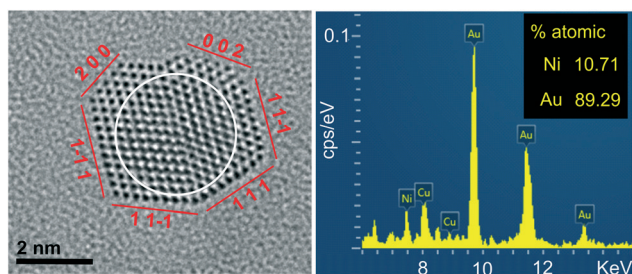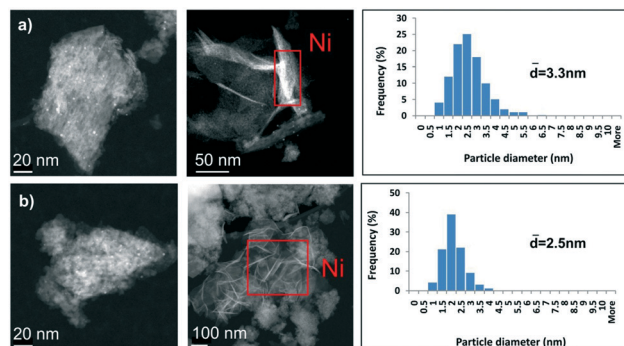

Fig. 6 STEM images and the respective histograms of a) Au–Ni$_{(DP)}$/γ-Al$_2$O$_{3(c)}$ and b) Au–Ni$_{(DP)}$/γ-Al$_2$O$_3$.

stand why the bimetallic Au–Ni catalysts outperform the monometallic ones, periodic density functional theory (DFT) calculations were performed focusing on the FA decomposition. TEM, XPS and ToF-SIMS analysis revealed the occurrence of strong Au–Ni interactions in bimetallic catalysts. Additionally, the existence of particles with a predominating amount of Au in the most active catalyst (Au–Ni$_{(CI)}$/γ-Al$_2$O$_{3(C)}$) was confirmed by TEM. In addition, it has been shown recently that a Ni–Au single atom alloy, where one Ni atom replaces one surface Au atom of a Au(111) surface, is accessible and exhibits a peculiar activity.[77] Thus, the Au–Ni bimetallic catalysts were modelled using a bimetallic surface in which one surface Au atom was replaced by one Ni atom (Fig. 7). In this model, Au atoms surround the Ni atom.

The decomposition of FA towards H$_2$ and CO$_2$ can proceed *via* two routes (Fig. 8). The carboxyl (COOH) route starts with C–H bond cleavage and continues with the OH one. The formate (HCOO) pathway starts with O–H bond breaking, yielding the very stable bidentate formate HCOO$_B$ intermediate. To further break the C–H bond, it is first necessary to break the metal–oxygen bond, yielding the formate monodentate HCOO$_M$ intermediate. Branching from the carboxyl intermediate COOH, a dehydration route is also possible through C–OH dissociation (Fig. 8). It produces water and CO, the latter being usually detrimental to the catalytic activity.

Three model surfaces were considered: Au(111), Ni(111) and Au–Ni(111) to investigate the impact of alloying on: (i) the dehydrogenation ability and (ii) the potential poisoning of CO.

As far as dehydrogenation is concerned, all the reaction intermediates and transition states of the formate pathway (Fig. 9) are more stable than those of the carboxyl pathway (Fig. S1†) for the three models under consideration. Thus, the formate pathway is clearly the most favoured one. This preference is also confirmed by the energetic span δG values (Table 4), which are lower for the dehydrogenation *via* the HCOO path. Energetic span δG can be described as the apparent activation energy for the catalytic cycle (see Computational details). The lower the energetic span, the faster the reaction.

The comparison of the energetic spans δG for monometallic Au and Ni and bimetallic Au–Ni surfaces (Table 4) shows

Fig. 5 HRTEM image and EDX spectrum of an isolated Au–Ni$_{(CI)}$/γ-Al$_2$O$_{3(c)}$ catalyst crystal.

4326 | *Catal. Sci. Technol.*, 2018, **8**, 4318–4331

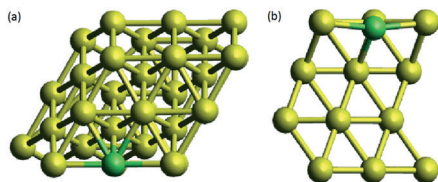This journal is © The Royal Society of Chemistry 2018

Fig. 7 Unit cell of the slab model used for the bimetallic Au–Ni surface – one Ni atom (in green) is embedded in the top layer surrounded by Au atoms (in yellow): (a) top view, (b) side view.

that the Au(111) surface is predicted to be barely active in comparison with Ni(111), with an energetic span ~0.8 eV higher. These results are in line with previous periodic DFT results on pure Au and pure Ni catalysts.[24,78,79] On the other hand, the energetic ranges for Ni and Au–Ni surfaces are comparable, with the alloy being predicted to be more active (Ni 1.59 eV $vs.$ 1.52 eV Au–Ni). In both cases, the decomposition is limited by the C–H bond scission. This step requires a pre-equilibrium between the bidentate formate $HCOO_B$ and the monodentate one $HCOO_M$. While the bidentate is over-stabilised on Ni(111), thanks to the formation of two strong Ni–O bonds, it is much less stabilised on the Au–Ni alloy, with the formation of a strong Ni–O bond and a weaker Au–O bond (for structures of HCOO, see Fig. 10; for the other structures among the pathways, see Fig. S2†). As a consequence, the monodentate formate is easier to achieve from the bidentate on the alloy surface than on the Ni one (δG = 0.57 eV for Au–Ni $vs.$ 0.96 eV for Ni). In contrast, the C–H dissociation step from the monodentate formate is more activated on the Ni–Au surface, hence moderating the overall effect. Last, looking at the adsorption of $1/2$ H_2 on the surfaces, it is stronger at the Ni surface than at the Au–Ni one (−0.90 eV $vs.$ −0.27 eV). Thus, not only the bidentate formate but also the H atoms may act as a 'poison' for the Ni surface. The latter is in line with the absence of activity of Ni in the levulinic acid hydrogenation experimentally observed.

Another source of poisoning is the production of CO by the dehydration of HCOOH. The corresponding energy profiles are gathered in Fig. S4.† Dehydration is not thermodynamically favoured in comparison with dehydrogenation, especially in liquid water. However, traces of CO could block the catalytic sites. Thus, the most important feature is the

fate of the CO traces that might be produced. On Au(111), CO should desorb very quickly since the desorption is stabilising. On Ni(111), CO is strongly chemisorbed in a hollow site with a desorption Gibbs free energy of 1.30 eV at 190 °C. This desorption energy is still lower than the energy span required to perform the dehydrogenation, meaning that CO should have only a limited detrimental effect on the catalytic performance. In the case of bimetallic Au–Ni, CO is adsorbed on the top of the isolated Ni atom. The alloying reduces the number of Ni–CO bonds and thus weakens the adsorption of CO (−0.96 eV). In addition, the reverse hydroxylation of CO into carboxyl COOH is competitive with the desorption with a barrier of 0.98 eV. Finally, COOH can be easily hydrogenated back to formic acid in the presence of H_2. In other words, even if CO can be produced on the Au–Ni alloy, it is not poisoning the catalytic site.

Discussion

In the hydrogenation of levulinic acid to γ-valerolactone with formic acid used as an internal hydrogen source obtained from FA decomposition, one of the challenges is to design a catalyst capable of performing both reactions under similar reaction conditions with high efficiency. The ability of a catalyst to perform this FALA reaction is tremendously impacted by the preparation method. The chemical reduction method provides the least active bimetallic catalyst, even if it still more active than the monometallic and benchmark catalysts. A calcination step followed by a high temperature reduction seems to be essential to ensure a high activity and the co-impregnation method appears to be the best synthesis strategy (see Table 1). The preparation method of the Au–Ni catalysts does not influence the direct hydrogenation of LA by H_2 significantly demonstrating that the FA decomposition is the key step in the FALA reaction.

When the FALA reaction is performed in a batch reactor, the autogenic H_2 pressure directly relies on the FA decomposition rate. A faster and more selective FA decomposition can result in a higher subsequent LA conversion, as this would promote a higher pressure. Additionally, the selective decomposition of FA to hydrogen and carbon dioxide while avoiding the formation of CO can protect the active sites from
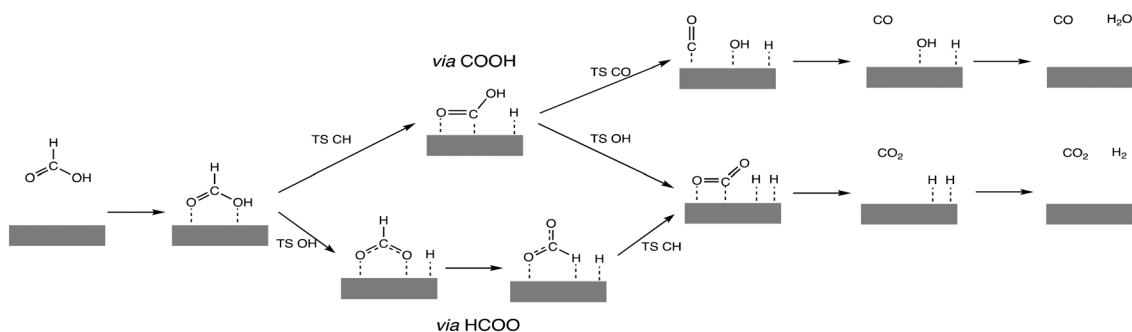

Fig. 8 Scheme of HCOOH decomposition: dehydration and dehydrogenation via carboxyl (top) and dehydration via formate (bottom) intermediates.
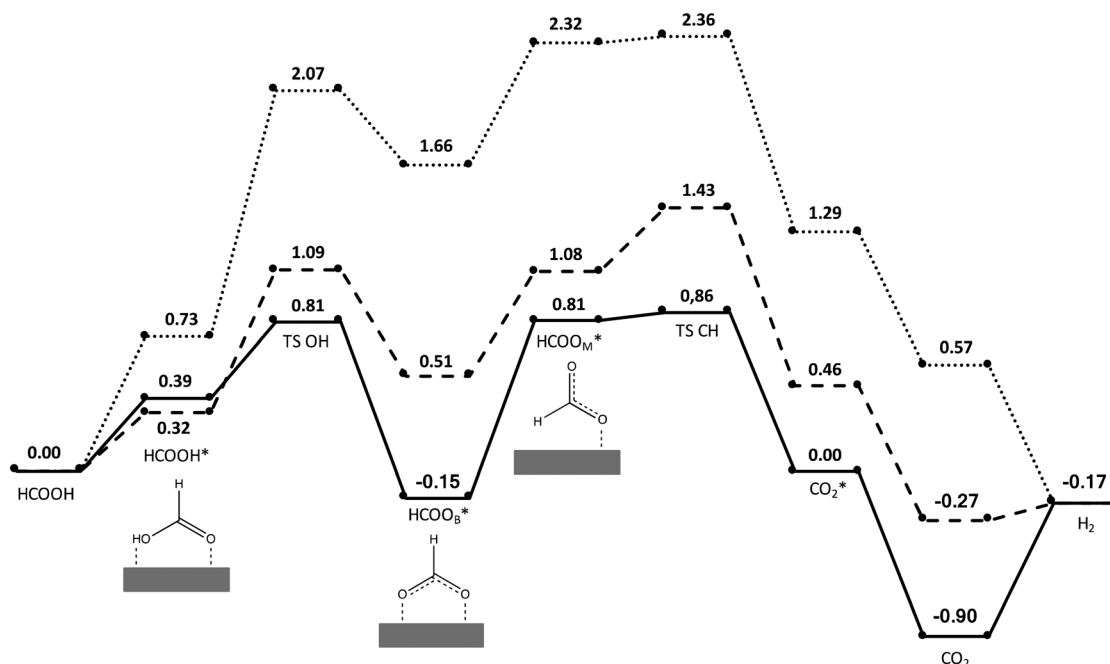
Fig. 9 HCOOH dehydrogenation *via* HCOO. Gibbs energy profiles for Au (dotted), Ni (plain), and Au–Ni bimetallic surfaces (dashed). Gibbs energies given in eV at *T* = 190 °C; * means adsorption at the surface.

poisoning by CO.[10] During the hydrogenation reaction with an internal hydrogen source, the FA decomposition is reported to occur first before the LA hydrogenation takes place.[10] So, it is of high importance to optimize the FA decomposition step, as both the conversion and the selectivity of this first reaction can directly influence the performance of the subsequent hydrogenation reaction towards GVL.

To rationalize the different activities that we observed, we combined the catalytic tests with structural characterizations and DFT computations.

The most active bimetallic catalyst possessed small particles of both metals in close contact, with an average particle size of 5.7 nm (TEM). The size of the crystallites is important, but even more the presence of the crystalline phase. Whereas the Au–Ni$_{(CI)}$/γ-Al$_2$O$_{3(C)}$ catalyst with the highest activity (GVL yield of 86%) has an average size of 5.7 nm, the Au–Ni$_{(DP)}$/γ-Al$_2$O$_{3(C)}$ sample with only a slightly lower activity (GVL yield of 72%) has nanoparticles with an average size of 3.3 nm, and the Au–Ni$_{(DP)}$/γ-Al$_2$O$_3$ catalyst with the smallest activity among these three has an average crystallite size of 2.5 nm. In the two latter samples, a significant contribution of the NiO$_x$ amorphous phase has however been observed, and is especially more pronounced in the lower activity catalyst, while such amorphous agglomerates have not been evidenced

in the TEM images of the most active catalyst. On the other hand the contribution of the crystalline phase of both metals on the surface of the Au–Ni$_{(CI)}$/γ-Al$_2$O$_{3(C)}$ catalyst is the highest among these three materials. This is also confirmed by XRD analysis, which showed a significant contribution of the Au metallic phase only for Au–Ni$_{(CI)}$/γ-Al$_2$O$_{3(C)}$ and Au/γ-Al$_2$O$_3$ catalysts. Also, the hydrogen uptake was the highest in the lower temperature region in the TPR profile of the Au–Ni$_{(CI)}$/γ-Al$_2$O$_{3(C)}$ catalyst. Judging from the ToF-SIMS estimation, the largest size of Au crystallites was observed for monometallic gold and the core shell sample containing the highest gold contribution on the surface. For other catalysts, the estimated size of gold nanoparticles that is presented as the Au$_2^-$/Au$^-$ ion intensity ratio remains much smaller and similar regardless of the catalyst. The smallest size of Au nanoparticles was estimated for the deposition–precipitation method, but as mentioned above the contribution of amorphous NiO$_x$ was significant in the Au–Ni$_{(DP)}$/γ-Al$_2$O$_{3(C)}$ catalyst.

Not only the presence of small crystallites of Ni and Au was beneficial, but also the existence of an interaction between

Table 4 Energetic spans δ*G* (in eV) for the HCOO and COOH routes in HCOOH dehydrogenation for Au, Ni, and Au–Ni surfaces

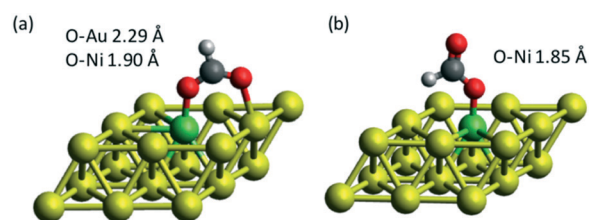|	Au	Ni	Au–Ni
via HCOO	2.36	1.59	1.52
via COOH	2.43	1.78	1.68

Fig. 10 Structures of (a) HCOO bidentate and (b) HCOO monodentate at the Au–Ni bimetallic surface.

both metals. The presence of this strong Au–Ni interaction was supported by HRTEM and EDX (with evidence of Ni atoms within well-defined Au nanocrystals), ToF-SIMS (with the record of Ni_2Au^- ions), XPS (with the observation of an energy shift towards higher energies for metallic Au) and TPR analysis (with a shift in the reduction temperature). We could also hypothesize that the strong decrease in the coherently-diffracting domain size observed for Au in Au–Ni bimetallic systems when compared to $Au/\gamma\text{-}Al_2O_3$ could result from the incorporation of Ni atoms within the Au nanoparticles. Also in the literature there are confirmations of this strong interaction in Au–Ni systems.[80,81]

The incorporation of Ni atoms within the Au nanoparticles modifies the reduction properties of Ni species, as well evidenced by TPR measurements. The highest hydrogen uptake was observed for the most active catalysts. The next section will further describe how the incorporation of Ni atoms plays a pivotal role in the ability of the catalyst to decompose FA.

Based on the convergent characterizations of the best Au–Ni catalyst, a model of the surface was built using a Au–Ni(111) surface, made of one surface Ni dissolved in a Au surface with a Ni : Au ratio of 1 : 9 (see Fig. 7). This model catalyst was compared with Au(111) and Ni(111) in terms of the ability to perform the FA decomposition using periodic DFT calculations. The dehydrogenation starts with the OH scission yielding the bidentate formate on all three surfaces. This intermediate is too stable on Ni(111) and too unstable on Au(111), limiting the reaction on these two catalysts. On the Au–Ni surface, the bidentate formate forms one strong Ni–O bond and a very weak Au–O bond, limiting its stability and favouring the overall reaction. In addition, hydrogen is less strongly chemisorbed on the alloy, which favours the H_2 production. Last, the traces of CO that might be generated by dehydration would strongly poison pure Ni catalysts since CO adsorbs strongly in hollow site. On Au–Ni, CO switches to atop site on isolated Ni atom, which weakens its adsorption energy and thus limits its poisoning power. All in all, the predicted activity in the FA decomposition is in line with the experimentally observed activity order (Au < Ni < Au–Ni) for catalysts prepared by the chemical reduction method, for which the interactions with the support are limited due to the absence of any reductive thermal treatment. The activity of monometallic gold towards FA decomposition is so negligible that it remains comparable with that of the bare Al_2O_3 support (shown in Table 1). This negligible activity of alumina was also confirmed in the literature.[82]

By contrast, applying a high temperature treatment resulted in the synthesis of Au catalysts with considerable activity in the FA decomposition. This is in agreement with the literature that reports that pure gold does not often show activity in the discussed reaction, although the presence of impurities or dopants like K can activate the gold nanoparticles.[83] Also it is known that the activity of gold depends strongly on the size of nanoparticles,[84] and that isolated Au species, strongly interacting with the $\gamma\text{-}Al_2O_3$ support, are able to promote FA decomposition while Au clusters are inactive.[85]

However, in both cases (thermal and chemical reduction), the bimetallic catalysts displayed a superior activity in the FA decomposition and the subsequent hydrogenation when compared to that of the monometallic counterparts. The presence of isolated well-reduced Ni atoms considerably enhances the FA decomposition according to our DFT study. The concentration of such actives sites tremendously depends on the preparation method. Since Au and Ni do not form a bulk alloy, the chemical reduction is too mild to allow the formation of a surface nano-alloy. The combination of calcination and high temperature reduction results in a bimetallic system that is more active than currently existing benchmark catalysts such as Ru/TiO_2 or Ru/ZrO_2 used for LA hydrogenation but with an external hydrogen source.[9,25]

Conclusions

To conclude, we demonstrated for the first time the high activity of bimetallic Au–Ni catalysts in the challenging transfer hydrogenation of LA with FA as an internal hydrogen source. The bimetallic $Au\text{–}Ni/\gamma\text{-}Al_2O_3$ catalysts strongly outperformed their monometallic counterparts, as well as the usual benchmark catalysts used for LA hydrogenation with external hydrogen. The performances shown by the bimetallic catalysts in the one-pot combined hydrogenation reaction were highly influenced by their preparation method, the highest GVL yield being achieved on the $Au\text{–}Ni/\gamma\text{-}Al_2O_3$ catalyst prepared *via* co-impregnation of both metallic salts.

The DFT study and extensive characterization of the bulk and surface properties of the catalysts were used for explaining the very high activity observed on the bimetallic Au–Ni systems. In particular, the existence of a strong Au–Ni interaction and the formation of a Au–Ni surface nano-alloy were put forward. The ability of the catalysts to rapidly perform the decomposition of FA in a selective way towards hydrogen is decisive for the efficiency of the one-pot hydrogenation reaction. Further, DFT calculations explained the role of Au and Ni, clearly showing that although monometallic Au catalysts do not favor the reaction, the presence of isolated metallic Ni atoms within the Au nanoparticles markedly lowers the reaction energetic span down to a value that is lower than that of pure metallic Ni. As a result of that, the reaction of selective FA decomposition into hydrogen is strongly facilitated, and consequently the subsequent combined hydrogenation process as well.

Conflicts of interest

There are no conflicts to declare.

Acknowledgements

This journal is © The Royal Society of Chemistry 2018

Catal. Sci. Technol., 2018, **8**, 4318–4331 | **4329**

'Hydrogen transfer reactions from biomass transformation'. Mimoun Aouine, Luis Cardenas and Francois Mirabel from IRCELYON (CNRS) are acknowledged for TEM and XPS measurements.

Notes and references

1 I. T. Horváth, H. Mehdi, V. Fábos, L. Boda and L. T. Mika, *Green Chem.*, 2008, **10**, 238–242.

2 D. M. Alonso, S. G. Wettstein and J. A. Dumesic, *Green Chem.*, 2013, **15**, 584–595.

3 J. P. Lange, R. Price, P. M. Ayoub, J. Louis, L. Petrus, L. Clarke and H. Gosselink, *Angew. Chem., Int. Ed.*, 2010, **49**, 4479–4483; J. P. Lange, R. Price, P. M. Ayoub, J. Louis, L. Petrus, L. Clarke and H. Gosselink, *Angew. Chem.*, 2010, **122**, 4581–4585.

4 D. J. Braden, C. A. Henao, J. Heltzel, C. C. Maravelias and J. A. Dumesic, *Green Chem.*, 2011, **13**, 1755–1765.

5 L. Corbel-Demailly, B. K. Ly, D. P. Minh, B. Tapin, C. Especel, F. Epron, A. Cabiac, E. Guillon, M. Besson and C. Pinel, *ChemSusChem*, 2013, **6**, 2388–2395.

6 W. Luo, U. Deka, A. M. Beale, E. R. van Eck, P. C. Bruijnincx and B. M. Weckhuysen, *J. Catal.*, 2013, **301**, 175–186.

7 M. G. Al-Shaal, W. R. Wright and R. Palkovits, *Green Chem.*, 2012, **14**, 1260–1263.

8 X. Liu, S. Li, Y. Liu and Y. Cao, *Chin. J. Catal.*, 2015, **36**(9), 1461–1475.

9 A. M. Ruppert, J. Grams, M. Jędrzejczyk, J. Matras-Michalska, N. Keller, K. Ostojska and P. Sautet, *ChemSusChem*, 2015, **8**(9), 1538–1547.

10 A. M. Ruppert, M. Jędrzejczyk, O. Sneka-Płatek, N. Keller, A. S. Dumon, C. Michel, P. Sautet and J. Grams, *Green Chem.*, 2016, **18**(7), 2014–2028.

11 M. Grasemann and G. Laurenczy, *Energy Environ. Sci.*, 2012, **5**(8), 8171–8181.

12 L. Deng, Y. Zhao, J. Li, Y. Fu, B. Liao and Q. X. Guo, *ChemSusChem*, 2010, **3**(10), 1172–1175.

13 J. Yuan, S. S. Li, L. Yu, Y. M. Liu, Y. Cao, H. Y. He and K. N. Fan, *Energy Environ. Sci.*, 2013, **6**(11), 3308–3313.

14 M. Varkolu, V. Velpula, D. R. Burri and S. R. R. Kamaraju, *New J. Chem.*, 2016, **40**(4), 3261–3267.

15 M. Varkolu, D. R. Burri, S. R. R. Kamaraju, S. B. Jonnalagadda and W. E. van Zyl, *Chem. Eng. Technol.*, 2017, **40**(4), 719–726.

16 P. P. Upare, M. G. Jeong, Y. K. Hwang, D. H. Kim, Y. D. Kim, D. W. Hwang, U. H. Lee and J. S. Chang, *Appl. Catal., A*, 2015, **491**, 127–135.

17 A. M. Hengne, A. V. Malawadkar, N. S. Biradar and C. V. Rode, *RSC Adv.*, 2014, **4**(19), 9730–9736.

18 W. Luo, M. Sankar, A. M. Beale, Q. He, C. J. Kiely, P. C. A. Bruijnincx and B. M. Weckhuysen, *Nat. Commun.*, 2015, **6**, 6540.

19 M. L. Testa, L. Corbel-Demailly, V. La Parola, A. M. Venezia and C. Pinel, *Catal. Today*, 2015, **257**, 291–296.

20 X. L. Du, L. He, S. Zhao, Y. M. Liu, Y. Cao, H. Y. He and K. N. Fan, *Angew. Chem., Int. Ed.*, 2011, **50**, 7815–7819.

21 B. Yang, R. Burch, C. Hardacre, G. Headdock and P. Hu, *ACS Catal.*, 2012, **2**(6), 1027–1032.

22 Z. Lijuan, T. Ruili, H. Pu, M. Yuru and X. Dingguo, *Xiyou Jinshu Cailiao Yu Gongcheng*, 2010, **39**(6), 945–948.

23 J. S. Yoo, F. Abild-Pedersen, J. K. Nørskov and F. Studt, *ACS Catal.*, 2014, **4**, 1226–1233.

24 J. Ftouni, A. Muñoz-Murillo, A. Goryachev, J. P. Hofmann, E. J. Hensen, L. Lu, C. J. Kiely, P. C. A. Bruijnincx and B. M. Weckhuysen, *ACS Catal.*, 2016, **6**, 5462–5472.

25 R. M. Bababrik, B. Wang and D. E. Resasco, *Ind. Eng. Chem. Res.*, 2017, **56**(12), 3217–3222.

26 M. Wąchała, J. Grams, W. Kwapiński and A. M. Ruppert, *Int. J. Hydrogen Energy*, 2016, **41**(20), 8688–8695.

27 G. Kresse and J. Hafner, *Phys. Rev. B: Condens. Matter Mater. Phys.*, 1993, **47**, 558–561.

28 J. P. Perdew, K. Burke and M. Ernzerhof, *Phys. Rev. Lett.*, 1996, **77**, 3865–3868.

29 S. N. Steinmann and C. Corminboeuf, *J. Chem. Phys.*, 2011, **134**, 044117.

30 S. N. Steinmann and C. Corminboeuf, *J. Chem. Theory Comput.*, 2011, **7**, 3567–3577.

31 S. Gautier, S. N. Steinmann, C. Michel, P. Fleurat-Lessard and P. Sautet, *Phys. Chem. Chem. Phys.*, 2015, **17**, 28921–28930.

32 P. E. Blöchl, *Phys. Rev. B: Condens. Matter Mater. Phys.*, 1994, **50**, 17953–17979.

33 G. Kresse and D. Joubert, *Phys. Rev. B: Condens. Matter Mater. Phys.*, 1999, **59**, 1758–1775.

34 H. J. Monkhorst and J. D. Pack, *Phys. Rev. B: Solid State*, 1976, **13**, 5188–5192.

35 http://cccbdb.nist.gov.

36 G. Henkelman, B. P. Uberuaga and H. J. Jonsson, *Chem. Phys.*, 2000, **113**, 9901–9904.

37 D. Sheppard, R. Terrell and G. J. Henkelman, *Chem. Phys.*, 2008, **128**, 134106.

38 P. Fleurat-Lessard, http://perso.ens-lyon.fr/paul.fleurat-lessard/ReactionPath.html, 2017.

39 G. Henkelman and H. Jonsson, *J. Chem. Phys.*, 1999, **111**, 7010–7022.

40 S. Kozuch and S. Shaik, *Acc. Chem. Res.*, 2011, **44**(2), 101–110.

41 S. Kozuch and M. L. Martin, *ChemPhysChem*, 2011, **12**, 1413–1418.

42 S. A. Nikolaev, E. V. Golubina, L. M. Kustov, A. L. Tarasov and O. P. Tkachenko, *Kinet. Catal.*, 2014, **55**, 311–318.

43 A. V. Chistyakov, P. A. Zharova, S. A. Nikolaev and M. V. Tsodikov, *Catal. Today*, 2017, **279**, 124–132.

44 A. Dong, J. Chen, P. Vora, J. Kikkawa and C. Murray, *Nature*, 2010, **446**, 474–477.

45 V. V. Kumar, G. Naresh, M. Sudhakar, C. Anjaneyulu, S. Kumar Bhargava, J. Tardio, V. Karnakar Reddy, A. H. Padmasri and A. Venugopal, *RSC Adv.*, 2016, **6**, 9872–9879.

46 S. Song, S. Yao, J. Cao, L. Di, G. Wu, N. Guan and L. Li, *Appl. Catal., B*, 2017, **217**, 115–124.

47 H. Reichert, A. Schops, I. B. Ramsteiner, V. N. Bugaev, O. Shchyglo, A. Udyansky, H. Dosch, M. Asta, R. Drautz and V. Honkimaki, *Phys. Rev. Lett.*, 2005, **95**, 235703–235707.

48 P. M. Holmblad, J. H. Larsen and I. Chorkendorff, *J. Phys. Chem.*, 1996, **104**, 7289–7295.

49 I. Sobczak, A. Kusior, J. Grams and M. Ziolek, *J. Catal.*, 2007, **245**, 259–266.

50 H. Tsai, E. Hu, K. Perng, M. Chen, J.-C. Wu and Y.-S. Chang, *Surf. Sci.*, 2003, **537**, L447–L450.

51 K. J. Kim and H. G. Ahn, *Appl. Catal., B*, 2009, **91**, 308–318.

52 C. K. Chang, Y. J. Chen and C. T. Yeh, *Appl. Catal., A*, 1998, **174**, 13–23.

53 S. Sang, Y. Wang, W. Zhu and G. Xiao, *Res. Chem. Intermed.*, 2017, **43**, 1179–1195.

54 M. Peymani, S. Mehdi and A. M. R. Peymani, *Appl. Catal., A*, 2017, **529**, 1–9.

55 C. P. Hwang and C. T. Yeh, *J. Mol. Catal. A: Chem.*, 1996, **112**, 295–302.

56 A. J. Akande, R. O. Idem and A. K. Dalai, *Appl. Catal., A*, 2005, **287**, 159–175.

57 Ch. Baatz, N. Thielecke and U. Prüsse, *Appl. Catal., B*, 2007, **70**, 653–660.

58 F.-W. Chang, L. S. Roselin and T.-C. Ou, *Appl. Catal., A*, 2008, **334**, 147–155.

59 F. Cárdenas-Lizana, S. Gómez-Quero, G. Jacobs, Y. Ji, B. H. Davis, L. Kiwi-Minsker and M. A. Keane, *J. Phys. Chem. C*, 2012, **116**, 11166–11180.

60 M. V. Bykova, D. Y. Ermakov, V. V. Kaichev, O. A. Bulavchenko, A. A. Saraev, M. Yu. Lebedev and V. A. Yakovlev, *Appl. Catal., A*, 2012, **113**, 296–307.

61 C. E. Dube, B. Workie, S. P. Kounaves, A. Rabbat, M. L. Aksu Jr. and G. Davies, *J. Electrochem. Soc.*, 1995, **142**, 3357–3365.

62 C. P. Li, A. Proctor and D. M. Hercules, *Appl. Spectrosc.*, 1984, **38**, 880–886.

63 V. Mohan, V. Venkateshwarlu, C. V. Pramod, B. D. Raju and K. S. R. Rao, *Catal. Sci. Technol.*, 2014, **4**, 1253–1259.

64 J. F. Moulder, W. F. Stickle, P. E. Sobol and K. D. Bomben, in *Handbook of X-ray Photoelectron Spectroscopy*, ed. J. Chastain, Perkin-Elmer Corporation, Norwalk, CT, 1992.

65 N. D. S. Canning, D. Outka and R. J. Madix, *Surf. Sci.*, 1984, **141**, 240–254.

66 A. Y. Klyushin, M. T. Greiner, X. Huang, T. Lunkenbein, X. Li, O. Timpe, M. Friedrich, M. Hävecker, A. Knop-Gericke and R. Schlögl, *ACS Catal.*, 2016, **6**, 3372–3380.

67 A. M. Visco, F. Neri, G. Neri, A. Donato, C. Milone and S. Galvagno, *Phys. Chem. Chem. Phys.*, 1999, **1**, 2869–2873.

68 S.-I. Naya, M. Teranishi, R. Aoki and H. Tada, *J. Phys. Chem. C*, 2016, **120**(23), 12440–12445.

69 S. Arii, F. Morfin, A. J. Renouprez and J. L. Rousset, *J. Am. Chem. Soc.*, 2004, **126**, 1199–1205.

70 J. Radnik, C. Mohr and P. Claus, *Phys. Chem. Chem. Phys.*, 2003, **5**, 172–177.

71 S. Schimpf, M. Lucas, C. Mohr, U. Rodemerck, A. Brückner, J. Radnik, H. Hofmeister and P. Claus, *Catal. Today*, 2002, **72**, 63–78.

72 B. Ealet and E. Gillet, *Surf. Sci.*, 1996, **367**, 221–230.

73 F. Cardenas-Lizana, S. Gomez-Quero, C. J. Baddeley and M. A. Keane, *Appl. Catal., A*, 2010, **387**, 155–165.

74 H. Nishikawa, D. Kawamoto, Y. Yamamoto, T. Ishida, H. Ohashi, T. Akita, T. Honma, H. Oji, Y. Kobayashi, A. Hamasaki, T. Yokoyama and M. Tokunaga, *J. Catal.*, 2013, **307**, 254–264.

75 S. Zafeiratos and S. Kennou, *J. Phys. Chem. B*, 2002, **106**(1), 41–48.

76 F. Cárdenas-Lizana and M. A. Keane, *Phys. Chem. Chem. Phys.*, 2015, **17**, 28088–28095.

77 Z. T. Wang, M. T. Darby, A. J. Therrien, M. El-Soda, A. Michaelides, M. Stamatakis and E. C. H. Sykes, *J. Phys. Chem. C*, 2016, **120**(25), 13574–13580.

78 Q. Luo, G. Feng, M. Beller and H. Jiao, *J. Phys. Chem. C*, 2012, **116**, 4149–4156.

79 J. A. Herron, J. Scaranto, P. Ferrin, S. Li and M. Mavrikakis, *ACS Catal.*, 2014, **4**, 4434–4445.

80 S. A. Nikolaev, A. V. Chistyakov, M. V. Chudakova, E. P. Yakimchuk, V. V. Kriventsov and M. V. Tsodikov, *J. Catal.*, 2013, **297**, 296–305.

81 S. De, J. Zhang, R. Luque and N. Yan, *Energy Environ. Sci.*, 2016, **9**, 3314–3347.

82 M. Ruan, H. Hou, W. Li and B. Wang, *J. Phys. Chem. C*, 2014, **118**, 20889–20898.

83 D. A. Bulushev, M. Zacharska, Y. Guo, S. Beloshapkin and A. Simakov, *Catal. Commun.*, 2017, **92**, 86–89.

84 J. Cheng, X. Gu, X. Sheng, P. Liu and H. Su, *J. Mater. Chem. A*, 2016, **4**, 1887–1894.

85 M. Ojeda and E. Iglesia, *Angew. Chem., Int. Ed.*, 2009, **48**, 4800–4803.

This journal is © The Royal Society of Chemistry 2018

Catal. Sci. Technol., 2018, **8**, 4318–4331 | **4331**